Unlocking the Stability of Reduced Graphene Oxide Nanosheets in Biological Media via Use of Sodium Ascorbate

Francesco Amato, Giordano Perini, Ginevra Friggeri, Alberto Augello, Alessandro Motta, Leonardo Giaccari, Robertino Zanoni, Marco De Spirito, Valentina Palmieri,* Andrea Giacomo Marrani,* and Massimiliano Papi

Graphene oxide and reduced graphene oxide (RGO) are carbon bidimensional nanomaterials largely exploited in biomedicine. Their unique interactions with eukaryotic and prokaryotic cells are used to obtain precise intracellular delivery, to create device coatings, and to design theranostic materials for both therapeutic and imaging applications, mainly in the cancer research field. It is known, however, that the hydrophobic behavior of RGO limits its stability in biological media. Here, the employment of sodium ascorbate (NaA) as a reducing agent for the preparation of RGO to provide a nanomaterial with remarkable suitability for applications in cell culture media is proposed. It is demonstrated via a combined experimental and theoretical approach that NaA is able to yield a peculiar RGO derivative, exerting a twofold effect, that is, C sp^2 network restoration upon epoxide reduction and RGO edge functionalization via H-bonding, lending RGO a so far unexampled dispersibility in aqueous-based media. The kinetic stability of the bidimensional layers of RGO obtained from NaA is demonstrated together with its superior biocompatibility for drug delivery, unlocking outstanding potentialities for biological applications.

1. Introduction

Since 2003, graphene-based materials have attracted considerable attention owing to their applications in medicine and interdisciplinary sciences.[1–3] Due to their bidimensional nature, nanomaterials like graphene and, more recently, MXenes have remarkable properties unknown to bacteria and eukaryotic cells, generating unprecedented biological responses. On one side, bidimensional materials have been studied to fight antimicrobial resistance and in general as antimicrobials, also against SARS-CoV-2 and other viruses.[4,5] On the other side, the possibility to deliver nucleic acids and drugs via the graphene surface inside eukaryotic cells has been largely investigated.[6,7]

Various synthetic routes so far reported, based on top-down and bottom-up approaches for the preparation of many classes of nanomaterials, can also be applied to graphene and its derivatives.[8,9] Each synthetic methodology displays both strengths and weaknesses in terms of reaction yield, purity, degree of induced structural defects, and handling of the sample. As an example, the top-down preparation of graphene through the exfoliation of graphite in the presence of surfactants affords mono and bilayers with a low number of structural defects. Yet, the limited reaction yield in addition to the necessary purification steps, limits large-scale applications of graphene.[10,11] Highly conductive and defect-free monolayers of graphene are also prepared through the well-investigated bottom-up chemical vapor deposition procedure.[12]

F. Amato, A. Motta, L. Giaccari, R. Zanoni, A. G. Marrani
Dipartimento di Chimica
Università di Roma La Sapienza
p.le A. Moro 5, Rome I-00185, Italy
E-mail: andrea.marrani@uniroma1.it

G. Perini, G. Friggeri, A. Augello, M. De Spirito, V. Palmieri, M. Papi
Dipartimento di Neuroscienze
Università Cattolica del Sacro Cuore
Largo Francesco Vito 1, Rome 00168, Italy
E-mail: valentina.palmieri@cnr.it
G. Perini, G. Friggeri, A. Augello, M. De Spirito, V. Palmieri, M. Papi
Fondazione Policlinico Universitario "A. Gemelli" IRCSS
Largo A. Gemelli, Rome 8 00168, Italy
A. Motta
Consorzio INSTM UdR Roma "La Sapienza"
p.le A. Moro 5, Rome I-00185, Italy
V. Palmieri
Istituto dei Sistemi Complessi
CNR
Via dei Taurini 19, Rome 00185, Italy

**ADVANCED
SCIENCE NEWS**

www.advancedsciencenews.com

**ADVANCED
MATERIALS
INTERFACES**
Open Access

www.advmatinterfaces.de

Despite the highly desirable features of the obtained layers of graphene, the limited ease of handling of the resulting product, including its poor water dispersibility, is a drawback for many types of applications, especially biological ones. Indeed, it is known that the hydrophobic behavior of some graphene-based materials limits their stability in biological media, which are rich in proteins and nutrients.[13]

Reduced graphene oxide (RGO), the material with the closest characteristics to graphene, is generally prepared from graphene oxide (GO) in the presence of chemical reducing agents, or via thermal and electrochemical treatments.[14,15] GO is the oxidized form of graphene, rich in oxygen-based functional groups, primarily hydroxyl and epoxide groups, which are mainly localized in the basal plane of the layer, while the less abundant carbonyl and carboxyl groups are confined at the edges.[16–19] These functionalities, arising from oxidative treatments of graphite, break the extended π-conjugation present in the layer, which is mainly responsible for the extraordinary physical-chemical properties of graphene.[20,21] In the preparation of RGO, the oxygen-based functionalities of GO can be strongly removed and the π-conjugation partially restored, yielding a material similar to graphene but with some structural defects, depending on both the reducing agent and the experimental conditions employed. In the literature, there are many examples of chemical reactions leading to GO reduction, carried out with different reducing agents, such as LiAlH$_4$, NaBH$_4$, L-cysteine, hydrazine, hydrohalic acids, N-acetylcysteine and L-ascorbic acid (AA), yielding RGO with various degree of deoxygenation.[22–25] In particular, AA is a mild reducing agent very frequently employed in the preparation of RGO, owing to its chemical safety, low-cost, and biocompatibility.[24–27] In fact, AA has been reported to attack the epoxide groups of GO in water, with the resulting partial restoration of the π-conjugated C sp^2 network.[24,27,28] Unfortunately, such a decrease in the content of polar oxygen-based functional groups and the concomitant increase of the π-conjugated islands, favor the aggregation of RGO layers or otherwise limit their colloidal kinetic stability in a wide range of pH and ionic strength.[29,30] In recent work, we explored the reaction mechanism of GO reduction exerted by AA with a combined theoretical and experimental approach, putting in evidence the AA dual reactivity toward both epoxide and edge carbonyl groups in GO.[24]

In this work, the reduction ability toward GO of sodium ascorbate (NaA), the conjugated base of AA, has been for the first time addressed and compared to its parent acidic form. Use of the sodium salt results in a highly water-dispersible nanomaterial which also retains the characteristics deriving from the extended π-electron delocalization of common RGO.

RGO-AA and RGO-NaA, the RGO nanomaterials obtained from the two syntheses, were characterized by means of morphological and spectroscopic techniques, while DFT-based calculations on the reduction mechanism shed light on the reasons for the peculiar effect of NaA. In addition, aggregation kinetics in cell culture media was addressed by cell viability tests and fluorescence microscopy, demonstrating that RGO-NaA is monodisperse even in rich media, and has higher stability compared to RGO-AA, paving the way for new biological applications of RGO.

2. Results and Discussion

2.1. AFM and DLS Characterization

The thickness of RGO nanosheets obtained after chemical reduction was characterized via AFM. The collected images display a large distribution of agglomerates with an average thickness of about four layers for RGO-AA (**Figure 1**a,c), differently from those prepared with NaA, in which isolated monolayers are clearly observed (Figure 1b,d).[31–33] The average lateral dimension of RGO sheets is 610 nm ± 70 nm for RGO-AA and 490 nm ± 50 nm for RGO-NaA (Figure 1e,f).

The hydrodynamic radius of nanomaterials was evaluated with dynamic light scattering (DLS), together with the surface charge by Zeta potential measurements. DLS data confirm that RGO-AA, with an average R_H of 356 nm ± 8 nm, has a larger size in water compared to RGO-NaA (average R_H of 246 ± 13 nm). Zeta potential is -26 ± 1 mV for RGO-AA compared to -42 ± 1 mV of RGO-NaA, which implies higher stability in water for the latter.

2.2. UV–Vis and Raman Spectroscopy Characterization

The UV–vis spectrum recorded on an aqueous dispersion of pristine GO (**Figure 2**, black line) displays the main peak localized at 232 nm and a shoulder at 300 nm, ascribable to π–π^* and n–π^* electron transitions, respectively.[23,34] The reduction of GO in the presence of AA yields a black powder with low water dispersibility (Figure S1, Supporting Information), differently from that obtained in the presence of NaA (Figure 2, red curve). In particular, in comparison to pristine GO, the UV–vis spectrum of RGO-NaA shows a red shift of the main band up to 272 nm, and the disappearance of the shoulder relative to n–π^* electron transitions as a consequence of the deoxygenation process.[23,24,27] Furthermore, an additional extensive absorption up to 800 nm is detected, as already reported for similar systems, due to the restoration of electronic conjugation within the basal plane of the material[35,36] (**Figure 3**).

The Raman spectrum of pristine GO shows the prominent D and G bands centered at $\approx$1362 cm^{-1} and $\approx$1604 cm^{-1} (**Figure 4**, black line), with an $I_D/I_G = 0.87$. These signals are relative to the ring-breathing mode from sp^2 carbon rings adjacent to an edge or defect and C–C stretching of sp^2 domains, respectively.[37] After reduction, the I_D/I_G ratio increases to 1.08 in RGO-AA, due to an increase of structural defect in the basal plane of the layer (Figure 4, blue line).[38,39] In the RGO-NaA sample (Figure 4, red line), the I_D/I_G ratio further increases to 1.14, suggesting the occurrence of a more effective reductive process.[23,24,37,40,41] According to the I_D/I_G values found, the mean distance among defects in the graphene layer, L_D, can be approximated to decrease from $\approx$12 nm in GO to $\approx$9 nm in RGO-NaA.[38,42] Notably, compared to pristine GO, the G band of both types of RGO is slightly red-shifted to $\approx$1594 cm^{-1}, and a new component D′ appears at $\approx$1610 cm^{-1}, as a result of the extensive reduction.[23,24,37,41,43–46]

2.3. X-Ray Photoelectron Spectroscopy Characterization

XPS spectroscopy was employed for the investigation of the surface functionalities of GO-based materials. The curve-fitted C
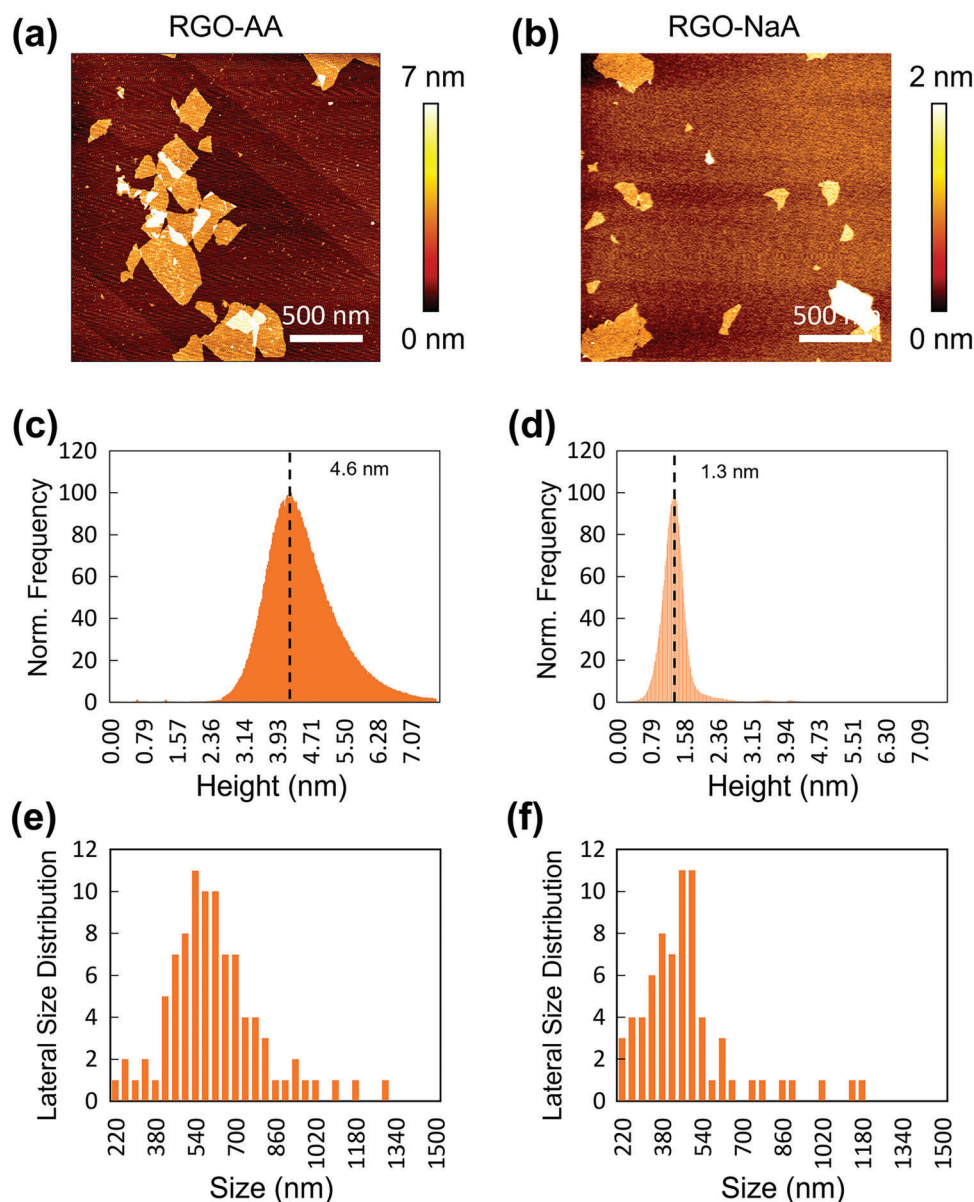
ADVANCED
SCIENCE NEWS

www.advancedsciencenews.com

ADVANCED
MATERIALS
INTERFACES
Open Access

www.advmatinterfaces.de

Figure 1. AFM-tapping mode images, statistical analyses of heights calculated after background subtraction and size distributions of RGO-AA (a,c,e) and RGO-NaA (b,d,f).

1s spectra of GO and its reduced derivatives are reported in Figure 4. The C 1s spectrum of pristine GO (**Figure 5**a) displays two main peaks, respectively ascribable to localized C_{sp2} domains at 284.8 eV (red curve) and a convolution of C–O bonds from hydroxyl (286.4 eV, blue curve) and epoxide (287.0 eV, green curve) groups.[46–48] The peak at higher binding energy is deconvoluted into two components, assigned to carbonyl/carboxylate groups, at 288.1 eV (magenta curves in Figure 5a), and to the less abundant carboxyl moieties at 289.2 eV (orange curves in Figure 5a).[46] The presence of such oxygenated carbon functional groups was confirmed also by FTIR spectroscopy (Figure S2, Supporting Information). Upon reduction with NaA (Figure 5b), a significant abatement of hydroxyl and epoxide groups is detected, with the corresponding normalized peak areas decreasing from 0.26 to

0.22 and from 0.75 to 0.05, respectively (**Table 1**). A similar drop in the epoxide groups signal can be found in RGO-AA (Figure 5c, 0.75 vs 0.06), whereas the amount of hydroxyl groups remains almost the same as in GO (0.27 vs 0.26).

In both RGO samples, a further component at 284.3 eV (brown curve in Figure 5b,c) is required for a proper curve-fitting of the C 1s region. This feature (C_{gr}) is slightly asymmetrical at its high binding energy side and accounts for an increased π-electron delocalization within the graphene plane upon the reduction reaction exerted by NaA and AA.[46,48–52] Noteworthy, this component is more intense in the case of RGO-NaA compared to RGO-AA (Figure 5d), calling at a more efficient restoration of the C_{sp2} network when NaA is used, consistently with the Raman data (Figure 4).
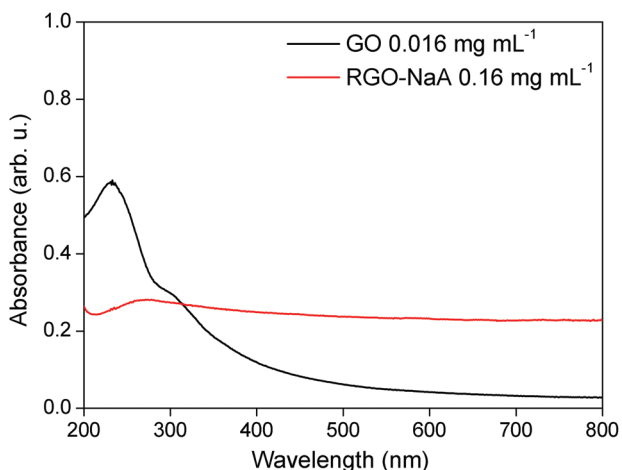
ADVANCED
SCIENCE NEWS

www.advancedsciencenews.com

ADVANCED
MATERIALS
INTERFACES
Open Access

www.advmatinterfaces.de

Figure 2. UV–vis spectra of GO (black line) and RGO-NaA (red line) recorded in water at room temperature. The corresponding concentrations are indicated.
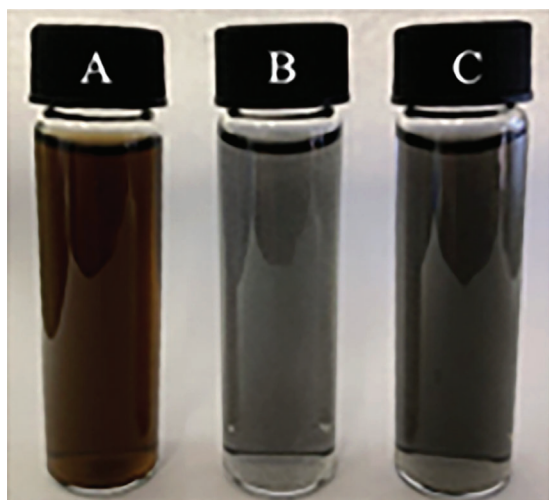

Figure 3. Aqueous dispersions at 0.5 mg mL^{-1} concentration of A) GO, B) RGO-AA, and C) RGO-NaA.

As to the possible presence of ascorbate residuals, their oxygenated C functional groups, in particular, C–OH and the lactone group –COO– are expected to contribute to the components at 286.4 and 289.2 eV, respectively.[53] In the spectrum of RGO-NaA (Figure 5b), the area of the latter component is seen to slightly increase compared to GO (Table 1), which supports the possibility of some type of ascorbate binding to RGO. In the case of RGO obtained from AA, the same experimental trend is seen, and we recently demonstrated with DFT theoretical calculations that one of the reduction routes actually leads to the covalent bond of this molecule to the edges of RGO sheets.[24]

XPS survey spectra displaying the whole ionization region are reported in Figures S3, S4 (Supporting Information) for RGO-AA and RGO-NaA, respectively. In the latter, the presence of Na can be detected, likely due to Na ions residuals.

2.4. Theoretical Modelling of Chemical Reduction Reaction of GO with NaA

The chemical reduction of GO with NaA has been scrutinized following the approach of the ascorbate reductant species (HA$^-$) on the GO surface. Only two oxidized species of the GO surface are considered for the reduction process, the basal epoxide and the edge carbonyl group.

When ascorbate (HA$^-$) approaches an epoxide group on the GO surface, a first electron transfer paralleled by a proton transfer occurs, producing a basal hydroxyl group and an ascorbate radical species (A$^{\bullet-}$). This step is spontaneous ($\Delta G = -9.2$ kcal mol^{-1}) and barrierless (**Figure 6**a).

A second electron transfer between an A$^{\bullet-}$ radical species and the surface could occur, leading to a C=C bond (pristine graphene) plus hydroxyl (OH$^-$) and dehydroascorbic acid (DHA) species, but this route is energetically disfavored (blue line on Figure 5a). By contrast, the approach of a second ascorbate anion produces water, pristine graphene, and A$^{\bullet-}$ radical species with the same mechanism of the first reduction step (Figure 5a). In this case, the step is very exergonic ($\Delta G = -58.5$ kcal mol^{-1}) and requires overcoming a low energy barrier ($\Delta G^{\ddagger} = +7.8$ kcal mol^{-1}) to occur. The proposed mechanism leads to the formation of the very stable A$^{\bullet-}$ radical species[54] and it strongly deviates from the epoxide reduction mechanism previously computed for ascorbic acid (AA).[24] Moreover, the overall epoxide reduction computed with the ascorbate species ($\Delta G = -67.7$ kcal mol^{-1}) is thermodynamically favored compared to the analog reduction computed with the ascorbic acid ($\Delta G = -57.7$ kcal mol^{-1}). This result is well tuned with the more efficient GO reduction exerted by NaA with respect to AA observed in XPS measurements.

On the other hand, when HA$^-$ approaches a carbonyl group at the edge of a GO layer, only one electron transfer plus a proton transfer occurs, producing a hydroxyl (enol) group and an A$^{\bullet-}$ radical species. The latter strongly remains bonded to GO via hydrogen bonding ($\Delta G = -34.5$ kcal mol^{-1}), unless an energy of 15.7 kcal mol^{-1} is provided for its removal. The HA$^-$ approach can also evolve to its covalent anchoring to the carbon atom vicinal to the carbonyl group (blue line in Figure 6b). In this case, the reaction is exergonic (-26.5 kcal mol^{-1}) and barrierless. This step leads to the formation of a new ether group bonded to a sp^3 carbon atom, without either any reduction or a proton transfer from ascorbate to GO. Overall, within the reaction mechanism involving the edge carbonyl group, the H-bonded A$^{\bullet-}$ radical species is the most stable intermediate, which, given its net negative electrical charge, may well explain the increased solubility of GO in water after treatment with NaA.

2.5. Stability of RGO-AA and RGO-NaA and Effects on RAW 264.7 Cell Viability

The use of RGO in biological applications involves the dissolution of the nanomaterial in media rich in proteins and nutrients, with consequent possible aggregation and instability. In **Figure 7**, we report the aggregation curves of RGO-AA (Figure 7a) and RGO-NaA (Figure 7b) in Dulbecco's modified Eagle's medium (DMEM), a largely employed medium for cell culture.
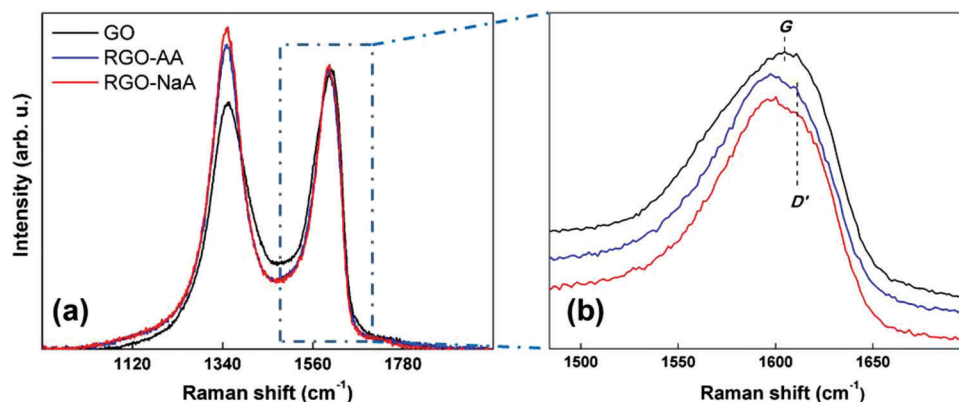
**ADVANCED
SCIENCE NEWS**

www.advancedsciencenews.com

**ADVANCED
MATERIALS
INTERFACES**

www.advmatinterfaces.de

Figure 4. a) Raman spectra of GO (black line), RGO-AA (blue line), and RGO-NaA (red line). b) Magnified portion of the spectrum in (a) in the region of G band.
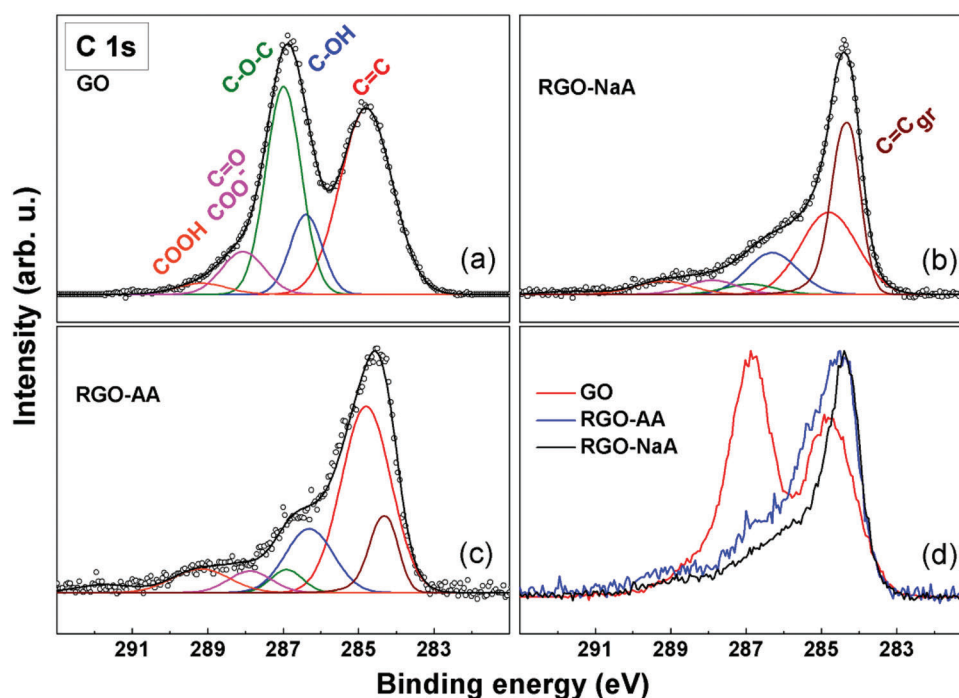

Figure 5. XPS spectra in the C 1s region of a) GO, b) RGO-NaA, c) RGO-AA. Experimental data are reported in dots, while curve-fitting results are reported with continuous colored lines, corresponding to different oxygenated functional groups. Raw data from the same spectra are overlapped in the (d) panel.

Aggregation has been followed measuring the OD for several hours (1000 min). As clearly visible, RGO-NaA is stable at all tested concentrations (12.5–100 µg mL^{-1}), while RGO-AA starts aggregating in the first 3 h at concentrations above 12.5 µg mL^{-1}.

This behavior has major consequences on the viability tests of the nanomaterials, since cells encounter large aggregates rather than single flakes. In **Figure 8**, the results of RAW 264.7 macrophage cell line viability assessment are displayed. After 24 h administration of RGO-AA or RGO-NaA using a concentration range between 12.5 and 100 µg mL^{-1}, the living cells were probed using the CellTiter-Glo Luminescence test and compared to untreated controls. As is visible from the graph in Figure 8a, cell viability using RGO-NaA is systematically higher, with a

Table 1. Area$^{a)}$ of relevant oxygenated functional groups in GO samples obtained from XPS C 1s spectra$^{b)}$.

Sample	C–OH	C–O–C	C=O + COO$^-$	COOH
GO	0.26	0.75	0.19	0.06
RGO-NaA	0.22^c	0.05	0.07	0.08^c
RGO-AA	0.27^d	0.06	0.08	0.12^d

$^{a)}$ Normalized to the sum of C$_{sp2}$ and C$_{gr}$ components; $^{b)}$ Associated error is ±10%; $^{c)}$ This value may be contributed also by ascorbate appended moieties; $^{d)}$ This value may be contributed also by ascorbic acid appended moieties.

**ADVANCED
SCIENCE NEWS**

www.advancedsciencenews.com

**ADVANCED
MATERIALS
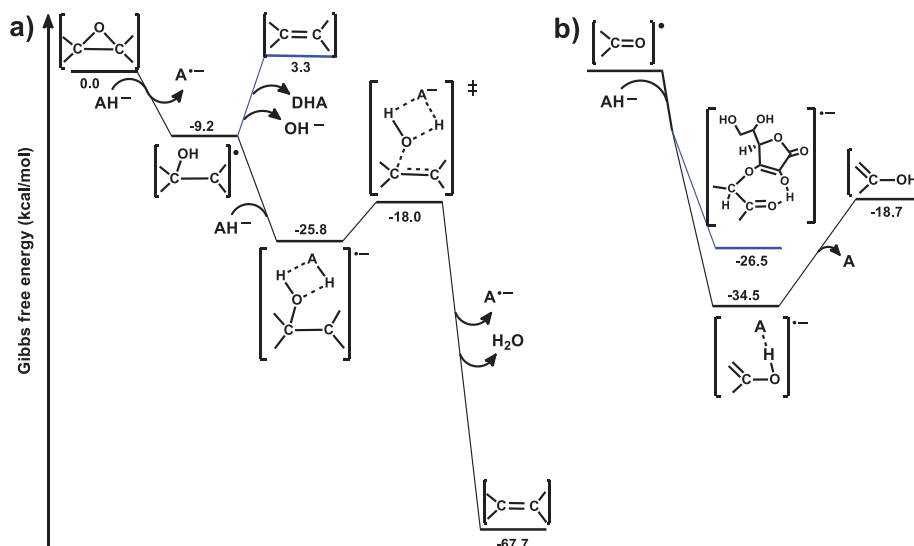INTERFACES**

www.advmatinterfaces.de

Figure 6. Computed mechanism of a) basal epoxy group reduction and b) carbonyl reduction at the edges of GO surface induced by HA⁻. Reaction Gibbs free energy (kcal mol⁻¹) values are also reported.
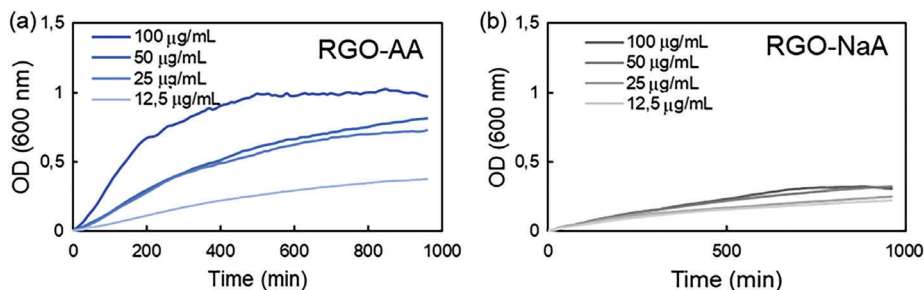

Figure 7. Aggregation kinetics of a) RGO-AA and b) RGO-NaA at different concentrations in DMEM cell medium. The reported values are an average resulting from three different samples tested and were performed in a concentration range of 12.5–100 µg mL⁻¹.
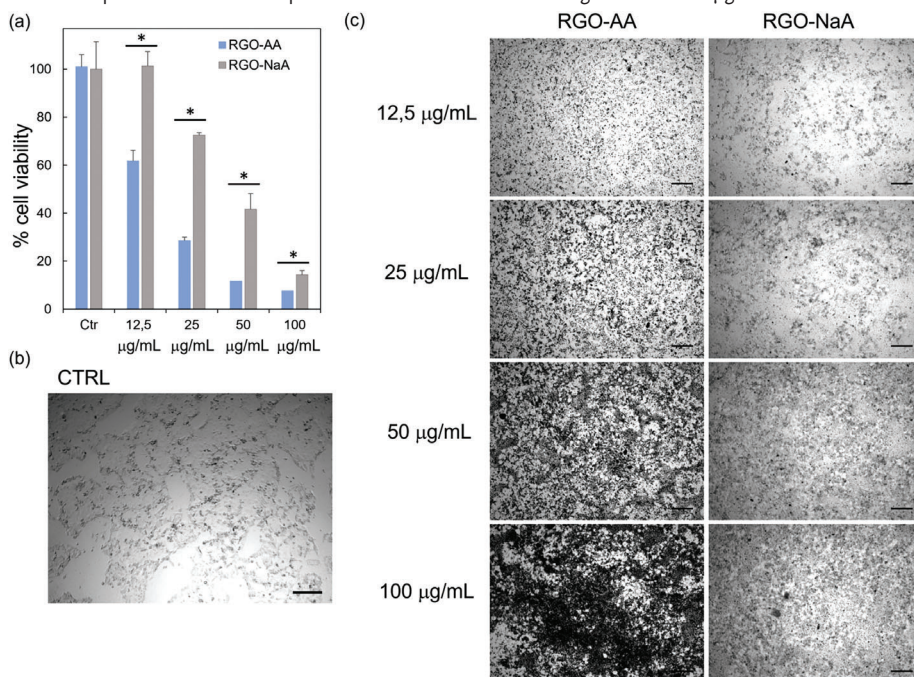

Figure 8. a) Cell viability test results after 24 h administration of RGO on RAW 264.7. Representative images obtained by optical microscopy of b) a CTRL sample and c) samples treated with an increasing concentration of RGO-AA or RGO-NaA. The scale bar in (b) and (c) is 200 µm.
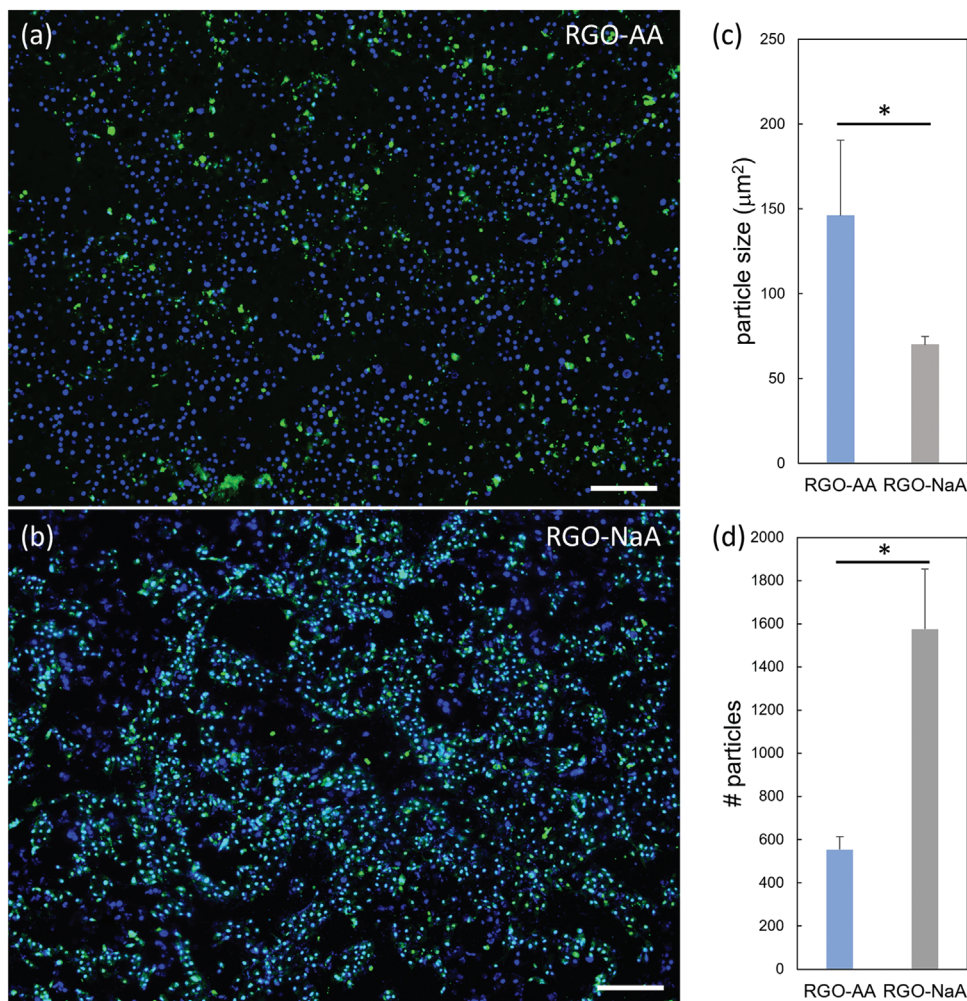
**ADVANCED
SCIENCE NEWS**

www.advancedsciencenews.com

**ADVANCED
MATERIALS
INTERFACES**
Open Access

www.advmatinterfaces.de

Figure 9. Fluorescence microscopy representative images of RGO-AA (a) and RGO-NaA (b) coated with FITC-albumin (green) and administered to RAW 264.7 cells labeled with DAPI (blue) and imaged with a 4× objective. The scale bar is 200 µm. Images were analyzed with ImageJ software and the average particle size (c) and particle number (d) were compared.

lack of cytotoxic effects at concentrations below 50 µg mL^{-1}. Conversely, cell viability is reduced with RGO-AA even at very low concentrations (12.5 µg mL^{-1}). At 50 µg mL^{-1}, RGO-NaA still shows ≈42% viability compared to ≈12% of RGO-AA. At 100 µg mL^{-1}, both types of RGO are toxic for this cell line. In Figure 8b,c, representative optical microscopy images of control and treated samples are displayed, respectively. Black aggregates are visible on RGO-AA images even at a low concentration (12.5 µg mL^{-1}), while in RGO-NaA aggregates appear only above 50 µg mL^{-1}, confirming the viability test results.

To evaluate the RGO distribution in the cells, RGO-AA and RGO-NaA were coated with FITC-Albumin and administrated at a concentration of 50 µg mL^{-1}, while cell nuclei were labeled with DAPI. Nanomaterial distribution was studied with Image analysis and is reported in graphs of **Figure 9**. In Figure 9a,b, a representative image of RGO-AA or RGO-NaA coated with FITC-Albumin and administered to cells is shown. Fluorescence microscopy and DAPI labeling were used to verify the distribution of RGO aggregates and to quantify the size and number of aggregates (Figure 9c,d). Images clearly show the uniform small

size of RGO-NaA compared to the large clumps of RGO-AA. The cyan color in Figure 9b demonstrates the co-localization of cell nuclei and RGO-NaA labeled with FITC-Albumin. Accordingly, the particle size of RGO-AA is twice larger than RGO-NaA, which is distributed throughout the sample with a higher number of smaller particles (Figure 9d). These data clearly demonstrate that RGO-NaA is more properly distributed within cells in terms of homogeneity and low aggregation, therefore it exhibits particularly advantageous potentiality in drug delivery applications.

3. Conclusion

The use of sodium ascorbate (NaA) as the reducing agent of GO was for the first time investigated here to attain a novel form of RGO, characterized by remarkable suitability for biomedical applications. We demonstrated that NaA exerts a twofold effect on the surface of GO: i) the C sp^2 network is efficiently restored upon epoxide reduction, as evidenced by spectroscopical (UV–vis, Raman, and XPS) measurements, and ii) the ascorbate molecule in its radical anion form (A$^{\bullet-}$) establishes a strong H-bonding

**ADVANCED
SCIENCE NEWS**

www.advancedsciencenews.com

**ADVANCED
MATERIALS
INTERFACES**

Open Access

www.advmatinterfaces.de

adduct with an edge hydroxyl enol group, as predicted by DFT theoretical computations. The resulting functionalization of RGO with ascorbate, due to the net negative charge of this latter, would be responsible for the so far unexampled dispersibility in the aqueous media of such a graphene derivative.

The kinetic stability of the RGO nanosheets obtained from NaA was assessed with optical density measurements in DMEM biological medium, demonstrating that it undergoes aggregation in water to a far lesser extent compared to that obtained from AA. This low aggregation capability unlocks its stability within cell culture media, allowing for better dispersion, cell entry, and lower cytotoxicity. The reported superior biocompatibility of this material may result particularly advantageous for its utilization in drug delivery and other biological applications.

4. Experimental Section

Reagents and solvents were purchased from Sigma–Aldrich, Fluka, Alfa Aesar, VWR, Euroclone, TCI and used as received, without further purification unless otherwise stated.

Synthesis of Nanomaterials: Pristine GO (GO) was synthesized by following a reported procedure, with some modifications.[34,55] Briefly, 69 mL of H_2SO_4 96 wt.% were added to a mixture of synthetic graphite (3.0 g) and $NaNO_3$ (1.5 g), and the mixture was cooled at 0 °C. Then, $KMnO_4$ (9.0 g) was added in portions and the mixture was stirred at 35 °C for 30 min. Subsequently, distilled water (138 mL) was added slowly and the mixture was heated at 98 °C for 15 min. Next, additional distilled water (420 mL) and H_2O_2 (3 mL, 30% v/v) were added. For workup, filtration through a filter paper was performed and the solid obtained was centrifuged at 4000 rpm for 30 min in the presence of HCl 1.12 м and distilled water (four times). During this step of purification, the supernatant was whenever discharged away and replaced with distilled water. Next, the solid was transferred to a round-bottom flask, then distilled water was added, and the mixture was stirred for one night to ensure proper exfoliation. Next, the dispersion was sonicated for 30 min and centrifuged at 3000 rpm for 40 min in order to recover the yellowish supernatant and discharge, as a precipitate, the graphite oxide that might be present. This procedure was repeated until the obtainment of an almost colorless supernatant. Finally, the dispersion of GO was dried under vacuum by means of a rotavapor at 35 °C, and the solid powder was stored in a desiccator.

Reduced graphene oxide from sodium ascorbate (RGO-NaA) was synthesized from GO. Briefly, 10 mL of an aqueous dispersion of GO 4.25 mg mL^{-1} was diluted to 50 mL of volume using distilled water. Then, 425 mg of sodium ascorbate (2.14 mmol) was added to the dispersion and the mixture was stirred at room temperature for 72 h. Subsequently, the mixture was centrifuged at 4000 rpm for 30 min in water (four times) discharging away the supernatant and keeping the solid black precipitate. Finally, the sample was dried under vacuum by means of a rotavapor at 35 °C and the solid powder was stored in a desiccator.

Reduced graphene oxide from L-ascorbic acid (RGO-AA) was synthesized in the same experimental conditions of RGO-NaA but in the presence of L-ascorbic acid (37 782 mg, 2.14 mmol) instead of sodium ascorbate.

Atomic Force Microscopy (AFM): AFM images were obtained by 100 μL of each sample (10 μg mL^{-1}) deposited on sterile mica slides and air-dried overnight. Images were acquired with a NanoWizard II (JPK Instruments AG, Berlin, Germany) using silicon cantilevers with high aspect-ratio conical silicon tips (CSC36 Mikro-Masch, Tallinn, Estonia) characterized by an end radius of ≈10 nm, a half conical angle of 20°, and a spring constant of 0.6 N m^{-1}. The average thickness was determined as a difference between the substrate peak value (set to zero) and the single flake GO peak, as reported previously.[56] Lateral size distribution was calculated using image analysis (FIJI software) from the square root of the flakes area.

UV–Vis and Raman Spectroscopy: UV–vis spectra were recorded with a Cary 500 UV–vis–NIR spectrophotometer. All spectra were recorded at room temperature using 10 mm path-length quartz cuvettes. Due to the different solubility of GO and RGO-NaA, the spectra of Figure 2 were recorded at different concentrations, for example, 0.016 mg mL^{-1} for GO and 0.16 mg mL^{-1} for RGO-NaA, with the former deliberately diluted in order to allow for visual comparison with the latter. Raman spectra were run at room temperature in backscattering geometry with an inVia Renishaw micro-Raman spectrometer equipped with an air-cooled CCD detector and super-Notch filters. An Ar$^+$ ion laser ($\lambda_{laser} = 514$ nm) was used, coupled to a Leica DLML microscope with a 20x objective. The resolution was 2 cm^{-1} and spectra were calibrated using the 520.5 cm^{-1} line of a silicon wafer. Raman spectra were acquired in several (6–10) different spots on the surface of the samples. For GO and its derivatives, each spectrum was acquired with 1% of power, 10 s of spectral acquisition, and 20 scans.

FTIR Spectroscopy: FTIR spectra were recorded by means of a micro-FTIR spectrophotometer LUMOS II Bruker in ATR mode. Measurements were performed on the powders of pristine GO, RGO, and ascorbic acid deposited onto glass slides. Each spectrum was collected with 96 scans, with a spectral resolution of 4 cm^{-1} and in the range of 4000–600 cm^{-1}.

X-Ray Photoelectron Spectroscopy (XPS): A freshly prepared H-terminated Si(100) surface was used as a support for the drop-casting of 50 μL of 0.06 mg mL^{-1} graphene derivative dispersions. XPS measurements were carried out using a modified Omicron NanoTechnology MXPS system equipped with a monochromatic Al Kα ($h\nu = 1486.7$ eV) X-ray source (Omicron XM-1000), operating the anode at 14 kV and 16 mA. The C1s photoionization region was acquired using an analyzer pass energy of 20 eV, while the survey spectra were acquired with a pass energy of 50 eV. A take-off angle of 21° with respect to the sample surface normal was adopted. The experimental spectra were theoretically reconstructed by fitting the secondary electrons' background to a Shirley function and the elastic peaks to pseudo–Voigt functions described by a common set of parameters: position, full-width at half-maximum, Gaussian–Lorentzian ratio. The relative amount of the different oxygenated functional groups was determined through the area of the peaks within the curve-fitting envelope of the C 1s region, with an uncertainty of ±10%.

Aggregation Kinetics, Dynamic Light Scattering (DLS), and Cell Viability: RGO-AA and RGO-NaA were dissolved at different concentrations in DMEM (Euroclone) and their aggregation kinetics was monitored by measuring the optical density (OD) at 600 nm using a Cytation 3 Multiplate Reader (Biotek, USA). The medium was composed of several molecules (aminoacids, proteins, glucose, lipids, salts, and many other components) that might induce aggregation of graphene oxide due to the formation of the protein corona on its surface.

DLS was carried out with a Zetasizer Nano S (Malvern Instruments, Malvern, UK) equipped with a 4 mW He–Ne laser (633 nm). Measurements were performed at a fixed angle of 173° with respect to the incident beam. Peak-intensity analyses were used to determine hydrodynamic radius number distribution (Pn) in different buffer conditions.

Murine macrophages (RAW 264.7 cell line) were cultured in DMEM supplemented with 10% inactivated fetal bovine serum (FBS) (Euroclone), 1% L-glutamine (Euroclone) and 1% streptomycin–penicillin (Euroclone) at 37 °C and 5% CO_2.

The cytotoxic effects of RGO were studied using a commercial CellTiter-Glo Luminescent Cell Viability Assay (Promega). Cellular viability was evaluated 24 h after the addition of RGO. The luminescence of the solution was determined using an automatic microplate reader, Cytation 3 Cell Imaging Multi-Mode Reader (Biotek Instruments). Each experiment was performed in triplicate. Cell imaging was obtained using a brightfield channel on Cytation 3 and a 4x objective.

RGO-AA and RGO-NaA were incubated with FITC-Albumin at a fixed concentration (1 mg mL^{-1}) for 1 h at 37 °C. Two centrifugation steps were performed to remove unbound protein (14 000 g) with resuspension in PBS. RGO-AA-FITC-Albumin and RGO-NaA-FITC-Albumin were administered to cells at a concentration of 50 μg mL^{-1}, after 24 h the cell medium was washed and replaced with a fresh one, while the cells were fixed for DAPI staining as previously reported. Imaging was performed using a
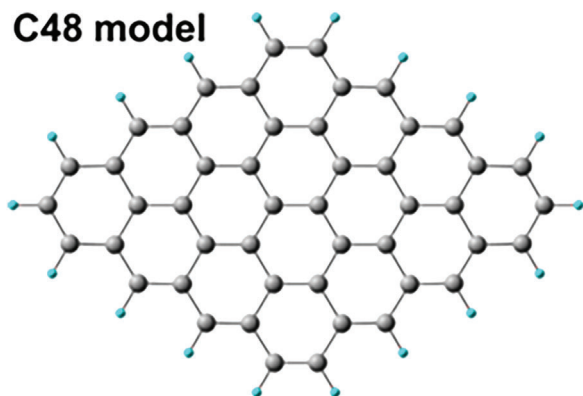
ADVANCED
SCIENCE NEWS

www.advancedsciencenews.com

ADVANCED
MATERIALS
INTERFACES

www.advmatinterfaces.de

Figure 10. The Graphene C48 cluster was used as a model in the DFT calculations.

4× objective of Cytation 3 Cell Imaging Multi-Mode Reader (Biotek Instruments).

Statistical Analysis: All data were represented as mean ± SD. Statistical analysis was performed using one-way ANOVA, followed by Tukey's post hoc test. Differences were considered significant when $p < 0.01$ and indicated with "∗".

DFT Calculations: Geometry optimizations of all reactants, products, intermediates, and transition states were carried out along the entire reduction reaction paths. Calculations were performed adopting the B3LYP hybrid GGA functional.[57] The standard all-electron 6–31G** double zeta basis set[58] plus polarization was used for all the atoms. Unrestricted calculations were always performed owing to an RHF/UHF instability verified in some cases. Molecular geometry optimization of stationary points was carried out without symmetry constrains and using analytical gradient techniques. The transition states were searched with the synchronous, transit-guided quasi-Newton method.[59] Frequency analysis was performed in order to verify stationary and saddle points and to obtain thermochemical information at standard conditions (298.15 K and 1 atm). Owing to the presence of anionic species among the intermediates, a single-point energy calculation with the addition of diffuse functions in the basis set was performed on the optimized geometry of all the investigated species. The force constants were determined analytically with the harmonic approximation. All calculations were performed using the G16 code[60] on Linux cluster systems. Molecular graphics were produced by the CHEMCRAFT graphical package.[61]

Pristine and oxidized graphene sheets were modeled adopting a hydrogen-passivated graphene cluster (**Figure 10**) of 48 carbon atoms (C48) as a starting point.[62]

Oxidized species were then appended on the basal plane and at the edges to model the local chemical environment on the graphene oxide sheet.

Supporting Information

Supporting Information is available from the Wiley Online Library or from the author.

Acknowledgements

Conflict of Interest

The authors declare no conflict of interest.

Data Availability Statement

The data that support the findings of this study are available from the corresponding author upon reasonable request.

Keywords

[1] T. P. Dasari Shareena, D. McShan, A. K. Dasmahapatra, P. B. Tchounwou, *Nano-Micro Lett.* **2018**, *10*, 53.
[2] V. Palmieri, M. Barba, L. Di Pietro, S. Gentilini, M. C. Braidotti, C. Ciancico, F. Bugli, G. Ciasca, R. Larciprete, W. Lattanzi, M. Sanguinetti, M. D. Spirito, C. Conti, M. Papi, *2D Mater.* **2017**, *5*, 015027.
[3] V. Palmieri, M. De Spirito, M. Papi, *Nanomedicine* **2020**, *15*, 1411.
[4] F. De Maio, V. Palmieri, M. De Spirito, G. Delogu, M. Papi, *Expert Rev. Med. Devices* **2019**, *16*, 863.
[5] F. De Maio, V. Palmieri, G. Babini, A. Augello, I. Palucci, G. Perini, A. Salustri, P. Spilman, M. De Spirito, M. Sanguinetti, *iScience* **2021**, *24*, 102788.
[6] V. Palmieri, L. Di Pietro, G. Perini, M. Barba, O. Parolini, M. De Spirito, W. Lattanzi, M. Papi, *Front. Bioeng. Biotechnol.* **2020**, *8*, 421.
[7] M. Daniyal, B. Liu, W. Wang, *Curr. Med. Chem.* **2020**, *27*, 3665.
[8] N. Kumar, R. Salehiyan, V. Chauke, O. Joseph Botlhoko, K. Setshedi, M. Scriba, M. Masukume, S. Sinha Ray, *FlatChem* **2021**, *27*, 100224.
[9] D. X. Luong, K. V. Bets, W. A. Algozeeb, M. G. Stanford, C. Kittrell, W. Chen, R. V. Salvatierra, M. Ren, E. A. McHugh, P. A. Advincula, Z. Wang, M. Bhatt, H. Guo, V. Mancevski, R. Shahsavari, B. I. Yakobson, J. M. Tour, *Nature* **2020**, *577*, 647.
[10] M. Cai, D. Thorpe, D. H. Adamson, H. C. Schniepp, *J. Mater. Chem.* **2012**, *22*, 24992.
[11] M. Lotya, Y. Hernandez, P. J. King, R. J. Smith, V. Nicolosi, L. S. Karlsson, F. M. Blighe, S. De, W. Zhiming, I. T. McGovern, G. S. Duesberg, J. N. Coleman, *J. Am. Chem. Soc.* **2009**, *131*, 3611.
[12] P. R. Unwin, A. G. Güell, G. Zhang, *Acc. Chem. Res.* **2016**, *49*, 2041.
[13] V. Palmieri, F. Bugli, M. C. Lauriola, M. Cacaci, R. Torelli, G. Ciasca, C. Conti, M. Sanguinetti, M. Papi, M. De Spirito, *ACS Biomater. Sci. Eng.* **2017**, *3*, 619.
[14] A. T. Dideikin, A. Y. Vul', *Front. Phys.* **2019**, *6*, 149.
[15] P. K. Jha, S. K. Singh, V. Kumar, S. Rana, S. Kurungot, N. Ballav, *Chem* **2017**, *3*, 846.
[16] D. R. Dreyer, S. Park, C. W. Bielawski, R. S. Ruoff, *Chem. Soc. Rev.* **2010**, *39*, 228.
[17] S. Eigler, A. Hirsch, *Angew. Chem., Int. Ed.* **2014**, *53*, 7720.
[18] S. Guo, S. Garaj, A. Bianco, C. Ménard-Moyon, *Nat. Rev. Phys.* **2022**, *4*, 247.

[19] V. Palmieri, F. Amato, A. G. Marrani, G. Friggeri, G. Perini, A. Augello, M. De Spirito, M. Papi, *Appl. Surf. Sci.* **2023**, *615*, 156315.

[20] O. C. Compton, S. T. Nguyen, *Small* **2010**, *6*, 711.

[21] H. Feng, R. Cheng, X. Zhao, X. Duan, J. Li, *Nat. Commun.* **2013**, *4*, 1539.

[22] C. K. Chua, M. Pumera, *Chem. Soc. Rev.* **2014**, *43*, 291.

[23] V. Palmieri, E. A. Dalchiele, G. Perini, A. Motta, M. De Spirito, R. Zanoni, A. G. Marrani, M. Papi, *Chem. Commun.* **2019**, *55*, 4186.

[24] A. G. Marrani, A. Motta, V. Palmieri, G. Perini, M. Papi, E. A. Dalchiele, R. Schrebler, R. Zanoni, *Mater. Adv.* **2020**, *1*, 2745.

[25] F. Amato, A. Motta, L. Giaccari, R. Di Pasquale, F. A. Scaramuzzo, R. Zanoni, A. G. Marrani, *Nanoscale Adv.* **2023**, *5*, 893.

[26] M. J. Fernández-Merino, L. Guardia, J. I. Paredes, S. Villar-Rodil, P. Solís-Fernández, A. Martínez-Alonso, J. M. D. Tascón, *J. Phys. Chem. C* **2010**, *114*, 6426.

[27] J. J. J. Zhang, H. Yang, G. Shen, P. Cheng, J. J. Zhang, S. Guo, *Chem. Commun.* **2010**, *46*, 1112.

[28] J. Gao, F. Liu, Y. Liu, N. Ma, Z. Wang, X. Zhang, *Chem. Mater.* **2010**, *22*, 2213.

[29] Y. Qi, T. Xia, Y. Li, L. Duan, W. Chen, *Environ. Sci.: Nano* **2016**, *3*, 1062.

[30] M. Moazzami Gudarzi, *Environ. Sci.: Nano* **2017**, *4*, 2418.

[31] H. C. Schniepp, J. L. Li, M. J. McAllister, H. Sai, M. Herrera-Alonson, D. H. Adamson, R. K. Prud'homme, R. Car, D. A. Seville, I. A. Aksay, *J. Phys. Chem. B* **2006**, *110*, 8535.

[32] C. Gómez-Navarro, R. T. Weitz, A. M. Bittner, M. Scolari, A. Mews, M. Burghard, K. Kern, *Nano Lett.* **2007**, *7*, 3499.

[33] K. Tsirka, A. Katsiki, N. Chalmpes, D. Gournis, A. S. Paipetis, *Front. Mater.* **2018**, *5*, 37.

[34] D. C. Marcano, D. V. Kosynkin, J. M. Berlin, A. Sinitskii, Z. Sun, A. Slesarev, L. B. Alemany, W. Lu, J. M. Tour, *ACS Nano* **2010**, *4*, 4806.

[35] D. Li, M. B. Müller, S. Gilje, R. B. Kaner, G. G. Wallace, *Nat. Nanotechnol.* **2008**, *3*, 101.

[36] M. K. Rabchinskii, V. V. Shnitov, A. T. Dideikin, A. E. Aleksenskii, S. P. Vul, M. V. Baidakova, I. I. Pronin, D. A. Kirilenko, P. N. Brunkov, J. Weise, S. L. Molodtsov, *J. Phys. Chem. C* **2016**, *120*, 28261.

[37] K. N. Kudin, B. Ozbas, H. C. Schniepp, R. K. Prud'homme, I. A. Aksay, R. Car, *Nano Lett.* **2008**, *8*, 36.

[38] S. Eigler, C. Dotzer, A. Hirsch, *Carbon* **2012**, *50*, 3666.

[39] I. K. Moon, J. Lee, R. S. Ruoff, H. Lee, *Nat. Commun.* **2010**, *1*, 73.

[40] A. Y. Lee, K. Yang, N. D. Anh, C. Park, S. M. Lee, T. G. Lee, M. S. Jeong, *Appl. Surf. Sci.* **2021**, *536*, 147990.

[41] A. G. Marrani, A. Motta, F. Amato, R. Schrebler, R. Zanoni, E. A. Dalchiele, *Nanomaterials* **2022**, *12*, 43.

[42] L. G. Cançado, A. Jorio, E. H. M. Ferreira, F. Stavale, C. A. Achete, R. B. Capaz, M. V. O. Moutinho, A. Lombardo, T. S. Kulmala, A. C. Ferrari, *Nano Lett.* **2011**, *11*, 3190.

[43] A. G. Marrani, R. Zanoni, R. Schrebler, E. A. Dalchiele, *J. Phys. Chem. C* **2017**, *121*, 5675.

[44] A. G. Marrani, A. Motta, R. Schrebler, R. Zanoni, E. A. Dalchiele, *Electrochim. Acta* **2019**, *304*, 231.

[45] A. G. Marrani, A. C. Coico, D. Giacco, R. Zanoni, F. A. Scaramuzzo, R. Schrebler, D. Dini, M. Bonomo, E. A. Dalchiele, *Appl. Surf. Sci.* **2018**, *445*, 404.

[46] I. Ferrari, A. Motta, R. Zanoni, F. A. Scaramuzzo, F. Amato, E. A. Dalchiele, A. G. Marrani, *Carbon* **2023**, *203*, 29.

[47] C. Y. Lin, C. E. Cheng, S. Wang, H. W. Shiu, L. Y. Chang, C. H. Chen, T. W. Lin, C. S. Chang, F. S. Sen Chien, *J. Phys. Chem. C* **2015**, *119*, 12910.

[48] R. Larciprete, P. Lacovig, S. Gardonio, A. Baraldi, S. Lizzit, *J. Phys. Chem. C* **2012**, *116*, 9900.

[49] G. Speranza, L. Minati, *Surf. Sci.* **2006**, *600*, 4438.

[50] M. R. C. Hunt, *Phys. Rev. B* **2008**, *78*, 153408.

[51] H. Estrade-Szwarckopf, *Carbon* **2004**, *42*, 1713.

[52] K. C. Prince, I. Ulrych, M. Peloi, B. Ressel, V. Cháb, C. Crotti, C. Comicioli, *Phys. Rev. B* **2000**, *62*, 6866.

[53] M. P. Briggs, D. Seah, *Practical Surface Analysis*, J. Wiley & Sons, Chichester, **1990**.

[54] Y. J. Tu, D. Njus, H. B. Schlegel, *Org. Biomol. Chem.* **2017**, *15*, 4417.

[55] J. Chen, Y. Li, L. Huang, C. Li, G. Shi, *Carbon* **2015**, *81*, 826.

[56] A. Liscio, K. Kouroupis-Agalou, X. D. Betriu, A. Kovtun, E. Treossi, N. M. Pugno, G. De Luca, L. Giorgini, V. Palermo, *2D Mater.* **2017**, *4*, 025017.

[57] A. D. Becke, *J. Chem. Phys.* **1993**, *98*, 5648.

[58] V. A. Rassolov, J. A. Pople, M. A. Ratner, T. L. Windus, *J. Chem. Phys.* **1998**, *109*, 1223.

[59] C. Peng, P. Y. Ayala, H. B. Schlegel, M. J. Frisch, *J. Comput. Chem.* **1996**, *17*, 49.

[60] M. J. Frisch, G. W. Trucks, H. B. Schlegel, G. E. Scuseria, M. A. Robb, J. R. Cheeseman, G. Scalmani, V. Barone, G. A. Petersson, H. Nakatsuji, et al., Gaussian 16 Revis. B.01 **2016**.

[61] "Chemcraft – graphical software for visualization of quantum chemistry computations", https://www.chemcraftprog.com (accessed: December 2022).

[62] D. Baniya, *Kathford J. Eng. Manage.* **2018**, *1*, 5.